Contents lists available at ScienceDirect

Applied Catalysis B: Environment and Energy

Modulating the precursors of carbon nitride to boost local electron delocalization for H_2O_2 photosynthesis to remove oxytetracycline and its antibiotic resistant genes

Zhi Li [a], Hao Lv [a], Kangbo Tong [b], Yupeng He [b], Chunyang Zhai [c], Yang Yun [b,*], Mingshan Zhu [a,*]

[a] Guangdong Key Laboratory of Environmental Pollution and Health, School of Environment, Jinan University, Guangzhou 511443, PR China
[b] College of Environment and Resource, Research Center of Environment and Health, Shanxi University, Taiyuan 030006, PR China
[c] School of Materials Science and Chemical Engineering, Ningbo University, Ningbo 315211, PR China

ARTICLE INFO

ABSTRACT

Artificial H_2O_2 photosynthesis, one of the brightest strategies toward H_2O_2 production, is always restricted by the intrinsically charge migration behaviors and redox kinetics of photocatalysts. Herein, different precursors of carbon nitride (C_3N_4) with urea and melamine (Mel) are synthesized, where C_3N_4-Urea has more delocalized electrons due to its smaller size and thickness, compared with C_3N_4-Mel. Under simulated sunlight irradiation, these abundant delocalized electrons rapid reduce oxygen into H_2O_2, with the rate of 4.9 mmol g^{-1} h^{-1} and 2e⁻ transfer selectivity of 98%. In addition, a self-photo-Fenton reaction system is constructed to remove oxytetracycline (OTC) pollutants and its antibiotic resistant genes (ARG) in water, with the degradation rate of 3.75 min^{-1} for OTC and 0.08 min^{-1} for tetC ARG. The current approach by modulating the precursors of C_3N_4 to boost the local electron delocalization offers a promising route for improving the efficiency of artificial H_2O_2 photosynthesis.

1. Introduction

Hydrogen peroxide (H_2O_2), a crucial green chemical, has wide-ranging applications across industry and environment field [1–4]. In the quest for sustainable alternatives to the energy-intensive traditional methods, such as anthraquinone oxidation method, H_2O_2 artificial photosynthesis has gained significant traction. This innovative approach involves the generation of H_2O_2 through reactions between O_2 and H_2O on the surface of photocatalyst, with eco-friendly, low-energy, and safe characteristics [5–7]. The crux of this endeavor lies in the efficiency of rate-determining step, including 2e⁻ oxygen reduction reaction (ORR) or water oxidation reaction (WOR), which relying greatly on the separation efficiency of photogenerated carriers. However, random charge flow resulted by rapid carrier recombination always restrain the efficiency of H_2O_2 photosynthesis [8–10]. Therefore, reducing photogenerated carrier complexation is vital to improve the efficiency of H_2O_2 photosynthesis.

Carbon nitride (C_3N_4) has become the most commonly used photocatalytic material to produce H_2O_2 due to its suitable energy band and excellent photocatalytic redox ability [11–13]. The pivotal influence of carbon-nitrogen atom hybridization within the π-conjugated structure highly determines the photoactivity of C_3N_4 [14]. On this basis, the prospect of fine-tuning π-conjugated system emerges as a fascinating avenue to improve the photoactivity of C_3N_4. Specially, intensified electron delocalization lead to a narrowing of the band gap and reinforces optical absorption, which is attributed to the up-shift of the highest occupied molecular orbital (HOMO) and the concurrent descent of the lowest unoccupied molecular orbital (LUMO) [15,16]. In addition, a composite system with large π delocalization can set up a charge transfer channel by hydrogen bonding [15] or π-π stacking interaction [17], which brings excellent photoactivity. The impact of electron delocalization stemming from π-π stacking interactions is invariably intertwined with the extent of exposed active sites on catalyst surface. Currently, the main methods to modulate electron delocalization of carbon nitride include structural engineering and morphology control [18,19]. Previous efforts have demonstrated that carbon nitride with different sizes and morphologies was obtained by adjusting different precursors [20]. Note that the content of delocalization electrons was highly determined by morphologies, thereby affecting the photocatalytic activity. However, little effort was used to enhance the electron

---

* Corresponding authors.
  E-mail addresses: yunyang@sxu.edu.cn (Y. Yun), zhumingshan@jnu.edu.cn (M. Zhu).

delocalization of carbon nitride by modulating the morphology.

Here, in contrast with previous efforts in this area [21,22], we use two different carbon-nitrogen precursors including melamine (Mel) and urea to synthesize C_3N_4 with different sizes of sheets and thicknesses. Note that smaller sheet and few-layer C_3N_4 is accompanied with more exposed area for delocalized electrons. Such abundant delocalized electrons are favorable to establish charge transfer channels; whereas larger sheet and multi-layer restrict the transfer of delocalized electrons [20,23]. Specifically, as demonstrated in Fig. 1-i, C_3N_4-Mel displays larger sheet and multi-layer, resulting in that interlayer and intra-sheet delocalized electrons are difficult to be utilized as electron transport channels. In contrast, C_3N_4-Urea has a smaller sheet and few-layer (Fig. 1-ii), which is very conducive to the exposure of delocalized electrons on the surface of material, allowing them to be used as electron transport channels. These abundant delocalized electrons can accelerate the separation of photogenerated carriers to achieve high production rate of H_2O_2. To understand the mechanism, atomic force microscopy (AFM), Kelvin probe force microscopy (KPFM), and single particles photoluminescence (PL) were carried out. In addition, in-situ self-photo-Fenton system are constructed to removal oxytetracycline (OTC) and its ARGs. This innovative approach provides a vital strategy to correlate the relationship between the surface delocalized electrons and the morphology of carbon nitride and offers an fire new understanding for H_2O_2 photosynthesis.

2. Materials and methods

The material, instruments, other experiments and characterizations are shown in Supplementary Information (Texts S1-S6).

2.1. Preparation of carbon nitride

Graphite carbon nitride (C_3N_4) was synthesized by thermal polymerization [24,25]. 10.0 g of urea and Mel powders was put into an Al_2O_3 crucible with a half-cover state. It was heated in a muffle oven at a rate of 10 °C min^{-1}, kept at a constant temperature for 3 h, and then cooled down to room temperature. Carbon nitride material at different temperatures including 400, 450, 500 and 550 °C using urea (viz. Urea 400 °C, Urea 450 °C, Urea 500 °C and Urea 550 °C) and 450, 500 and 550 °C using Mel (viz. Mel 450 °C, Mel 500 °C and Mel 550 °C) were synthesized. These samples were sonicated for 30 min to form nanosheets, prior to photocatalytic measurement. C_3N_4-Dicyandiamide (DCD) was synthesized by same thermal polymerization.

2.2. Apparent quantum efficiency measurements

Apparent quantum efficiency (AQE) measurements: For AQE measurements, 10 mg of photocatalyst was dispersed in 20 mL of 10 vol% EtOH. A 300 W Xe-lamp with a band-pass filter of 380 ± 15, 420 ± 15, 450 ± 15, 500 ± 15, 550 ± 15, 600 ± 15 or 650 ± 15 nm was used as the incident light source. The light intensity was adjusted to be 4.52, 3.13, 3.64, 6.23, 7.07, 6.68 and 7.74 mW cm^{-2}, respectively. The irradiation area was controlled to be 4 cm^2. The amount of H_2O_2 production was analyzed after 1 h irradiation. AQE was calculated using the following equation:

$$AQE\% = 2 \times (N_{H2O2}\, N_A\, h\, c) / (I\, S\, t\, \lambda) \times 100\%$$

where N_{H2O2} was the amount of H_2O_2 production (mol), N_A was the Avogadro constant (6.022×10^{23} mol^{-1}), h was the Planck constant (6.626×10^{-34} J s), c was the speed of light (3×10^8 m s^{-1}), I was the irradiation intensity (W cm^{-2}), S was the irradiation area (cm^2), t was the irradiation time (s) and λ was the wavelength of incident light (m) [26].

2.3. Product inactivation of bacteria in vitro

Bacterial inactivation experiments were subsequently carried out using generated H_2O_2 after filtering the photocatalyst particles. The filtrate solution containing generated H_2O_2 was taken every 10 min for adding to the bacterial suspension. Single *S. aureus* (MRSA) (186335 BNCC) colony was diluted with Luria Bertani (LB) medium and different time of product to approximately 1×10^5 CFU mL^{-1}. The bacterial suspension (200 µL) was seeded at the culture well and data were then collected at 2 h intervals for 12 h while maintaining the temperature at 37 °C [27]. Similarity, the bacteria were diluted to 1×10^7 CFU mL^{-1} with 0.85% NaCl solution and product in 5 mL tubes for half day, and 100 µL bacterial solution was taken to coat plate and the plate was incubated for 24 h at 37 °C. The bacterial live/dead staining was undertaken followed the manufacture's protocol (S34854 Thermo Fisher Scientific, 25535 SIGMA ALDRICH) and fluorescent images were taken on a microscope (TH4–200, OLYMPUS). The protein leakage, adenosine triphosphate (ATP) activity, protein oxidation, and lipid oxidation of bacteria were tested according to the kits (PC0020 Solarbio, BC1275 Solarbio, BC0025 Solarbio, BC0305 Solarbio).

2.4. Degradation of OTC and its antibiotic resistant genes

100 mL water samples were collected from OTC reaction and suction filtrated with 0.22 µm sterilized PES membrane. According to the
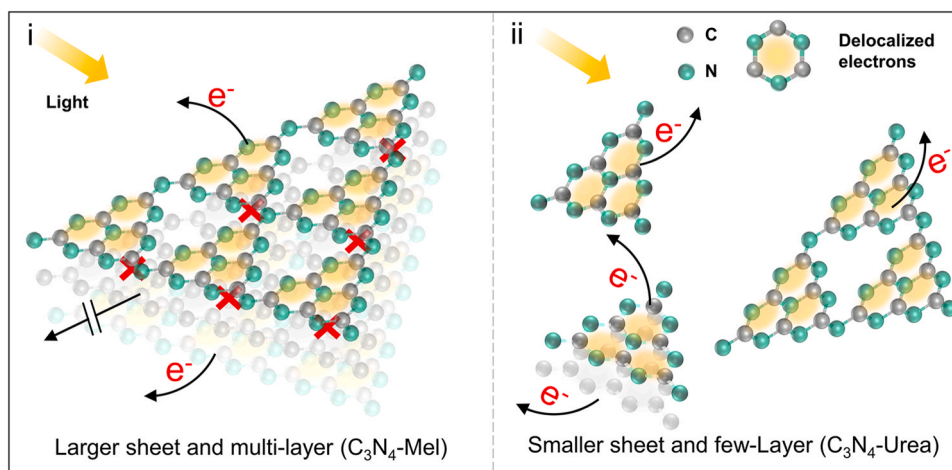

Fig. 1. Scheme for delocalized electrons of carbon nitride: larger sheets and multi-layers (i) and smaller sheets and fewer layers (ii) of carbon nitride.

manufacturer's instructions, genome DNA was extracted using a Power-Water DNA extraction kit (14900,Qiagen). The purity and concentration of the obtained DNA were determined using microvolume spectrophotometry (NanoDrop 2000, Thermo Fisher Scientific) and qubit (Qubit™4 flutermeter, Thermo Fisher Scientific).

The amplification of ARGs was performed using a PCR gene amplification instrument (PTC-1148, Bio-RAD). The PCR amplification reaction was carried out in a 20 μL reaction mixture, including 1 ng DNA template,1 μL forward and reverse primers (10 μM) respectively, 10 μL PCR Master Mix (208054,Qiagen) and replenish to 20 μL with sterilized Triple distilled water. PCR products were stored at 4 °C or next DNA gel electrophoresis, detected and removal experiments. The primers and processes used in this study are listed in Supplementary Information (Table S1). DNA gel electrophoresis was performed with 5 μL templets and the results were observed and obtained via Image Lab software (Bio-RAD imager, Bio-RAD ChemiDoc XRS).

The degradation of OTC was conducted in the continuous-flow reactor under visible light irradiation. All reactions were performed in a 100 mL solution (pH=3) contained 50 mg L^{-1} OTC or 20 mg L^{-1} $_{ARG}$, 0.5 g L^{-1} Urea 450 °C and 0.4 mM Fe_2SO_4. At certain time intervals, the reaction samples were periodically withdrawn and immediately quenched with excess $Na_2S_2O_3$ then filtered into a vial for analysis. The samples were taken in the outflow within 10 min intervals and immediately quenched with excess $Na_2S_2O_3$, then filtered and analyzed. HPLC with an Agilent SB-C18 column (2.1 mm × 100 mm, 1.8 μm) and an UV detector was used to analyze the concentration of OTC. The corresponding volume ratios of acetonitrile and 0.1% formic acid were 20:80 at peak of 365 nm for OTC. PCR and DNA gel electrophoresis were used to analyze the degraded ARGs concentration and purity.

3. Results and discussion

C_3N_4-Urea and C_3N_4-Mel were synthesized via a thermal polymerization process in Fig. S1. X-ray diffraction (XRD) pattern displays two obvious diffraction peaks at 12.7° and 27.2°, corresponding to the (100) and (002) planes of C_3N_4, respectively (Fig. S2) [28]. These two peaks are attributed to in-plane structural ordering and interlayer stacking peaks in graphite materials (Fig. S3) [29,30]. Compared to Mel 550 °C, these diffraction peaks in (100) and (002) are drastically reduced, suggesting a decrease in intra-layer periodic ordering and inter-layer stacking in Urea. XRD patterns of other samples are also shown in Fig. S4.
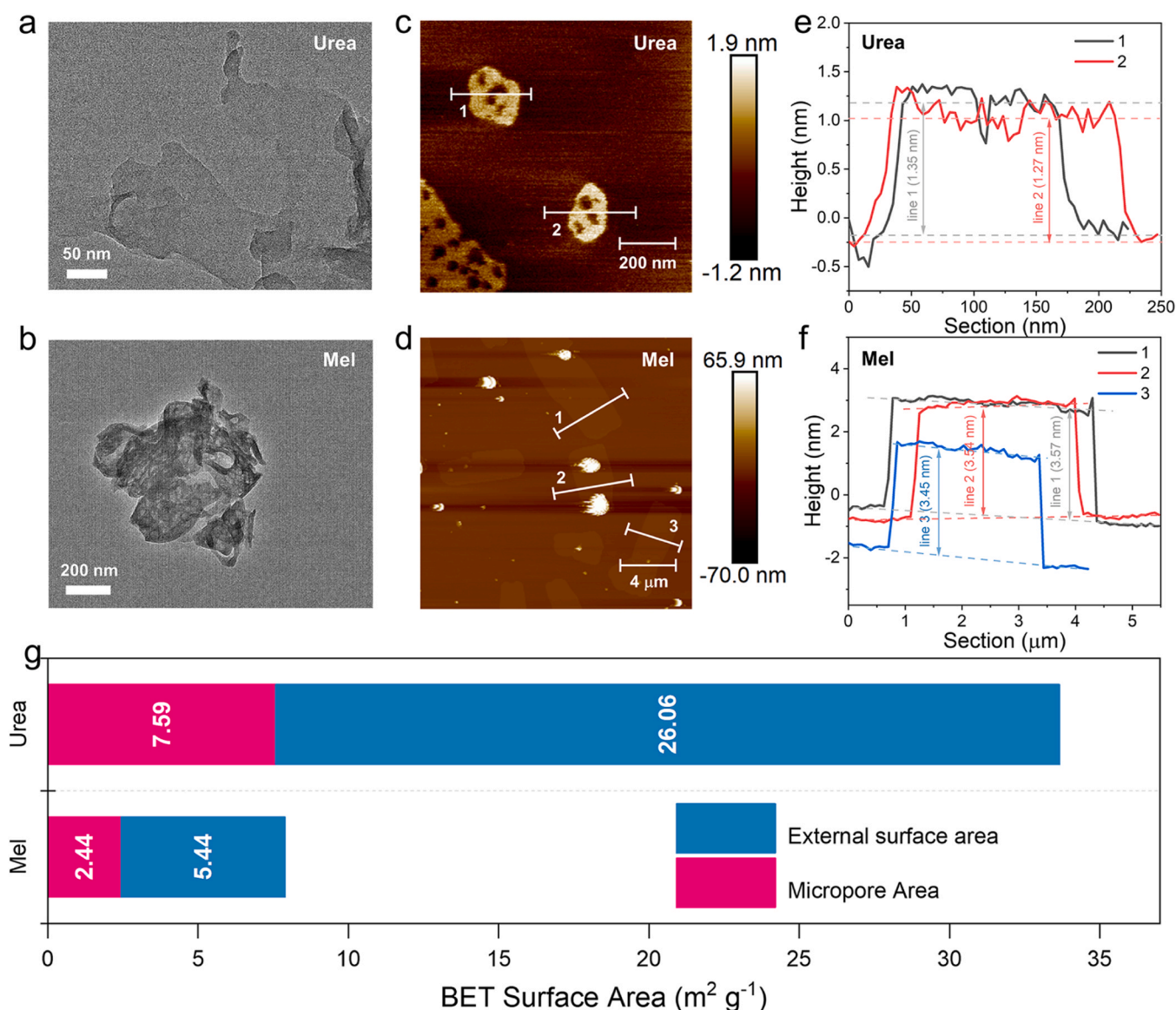

Fig. 2. TEM images (a and b), AFM images (c and d), the corresponding height image (e and f) and specific surface area distribution (g) of C_3N_4-Urea and C_3N_4-Mel.

The chemical bond features of C_3N_4-Urea and C_3N_4-Mel were investigated using Fourier transform infrared spectroscopy (FT-IR) (Fig. S5). Both C_3N_4-Urea and C_3N_4-Mel exhibited two peaks at 809 and 892 cm^{-1}, attributing to the condensed C-N heterocycles from triazine moiety, and the peaks at 1200–1700 cm^{-1} are corresponding to the stretching modes of C-N heterocycles from triazine [31]. A novel peak at 2180 cm^{-1} for C_3N_4 is ascribed to cyano groups (-C≡N) from melon structural unit. All samples show a broad band at 3200–3400 cm^{-1} owing to the terminal amino group and the presence of H_2O [32]. FT-IR spectra of other samples are also shown in Fig. S6.

The morphological and thickness of C_3N_4-Urea and C_3N_4-Mel were meticulously elucidated through transmission electron microscopy (TEM) and AFM images. As illustrated in Fig. 2a and b, both C_3N_4-Urea and C_3N_4-Mel presented as 2D nanosheets, with C_3N_4-Urea exhibiting notably superior dispersion and a significantly reduced thickness in comparison to C_3N_4-Mel. This divergence in thickness was corroborated by the AFM data presented in Fig. 2c, d, e and f, revealing average thicknesses of 1.31 nm (approximately equivalent to three C−N layers) for C_3N_4-Urea and 3.52 nm (approximately equivalent to eleven C−N layers) for C_3N_4-Mel. These observations underscore the substantially smaller, few-layered nature of C_3N_4-Urea in contrast to the larger, multi-layered structure of C_3N_4-Mel. The nitrogen adsorption–desorption isotherms and Barrett–Joyner–Halenda (BJH) pore-size distributions of C_3N_4 samples, prepared from different precursors are depicted in Fig. S7. These isotherms, classified as type IV(BDDT classification), show the presence of mesopores across two samples [33]. The specific surface area (33.65 m^2 g^{-1}) of C_3N_4-Urea is significantly greater than that

(7.88 m^2 g^{-1}) of C_3N_4-Mel, and the details of surface area distribution are summarized in Fig. 2g. These fully demonstrate that C_3N_4-Urea has more pores and larger specific surface area. The optical properties were explored by ultraviolet-visible (UV—Vis) absorption spectra, demonstrating the absorption edge of 470 nm and 440 nm, respectively (Fig. S8). In comparison to Mel 550 °C, Urea 450 °C shows a slight blue shift in the absorption edge, due to incomplete polymerization caused by low temperatures [22], and that of other samples are also shown in Fig. S9.

The unpaired electrons were investigated by Electron paramagnetic resonance (EPR) spectroscopy (Fig. 3a and b). All the samples showed a single Lorentzian line with g = 2.0042, corresponding to the delocalized electrons on the heptazine rings [34]. Mel 550 °C and Urea 450 °C demonstrated high delocalized electrons content and, in particular, Urea 450 °C exhibits the highest increase in delocalized electrons concentration under visible light, relative to that w/o light (Fig. 3c). These results fully prove that Urea 450 °C displays the largest number of delocalized electrons and can be further increased under light, which is highly favorable for photogenerated carrier migration.

To investigate the role of delocalized electrons in photocatalytic H_2O_2 production, C_3N_4 with different precursors were used to be placed in the reactor under visible light. As shown in Fig. 4a and S10, the performance of C_3N_4-Urea and C_3N_4-Mel follows the sequence: Urea 450 °C > Urea 400 °C > Urea 500 °C > Urea 550 °C > Mel 550 °C > Mel 500 °C > Mel 450 °C, and the performance of H_2O_2 production of C_3N_4-Dicyandiamide (DCD) are also shown in Figs. S10c and S11. Interestingly, the H_2O_2 yield of Urea 450 °C (1.58 mmol g^{-1} h^{-1}) is 2.33
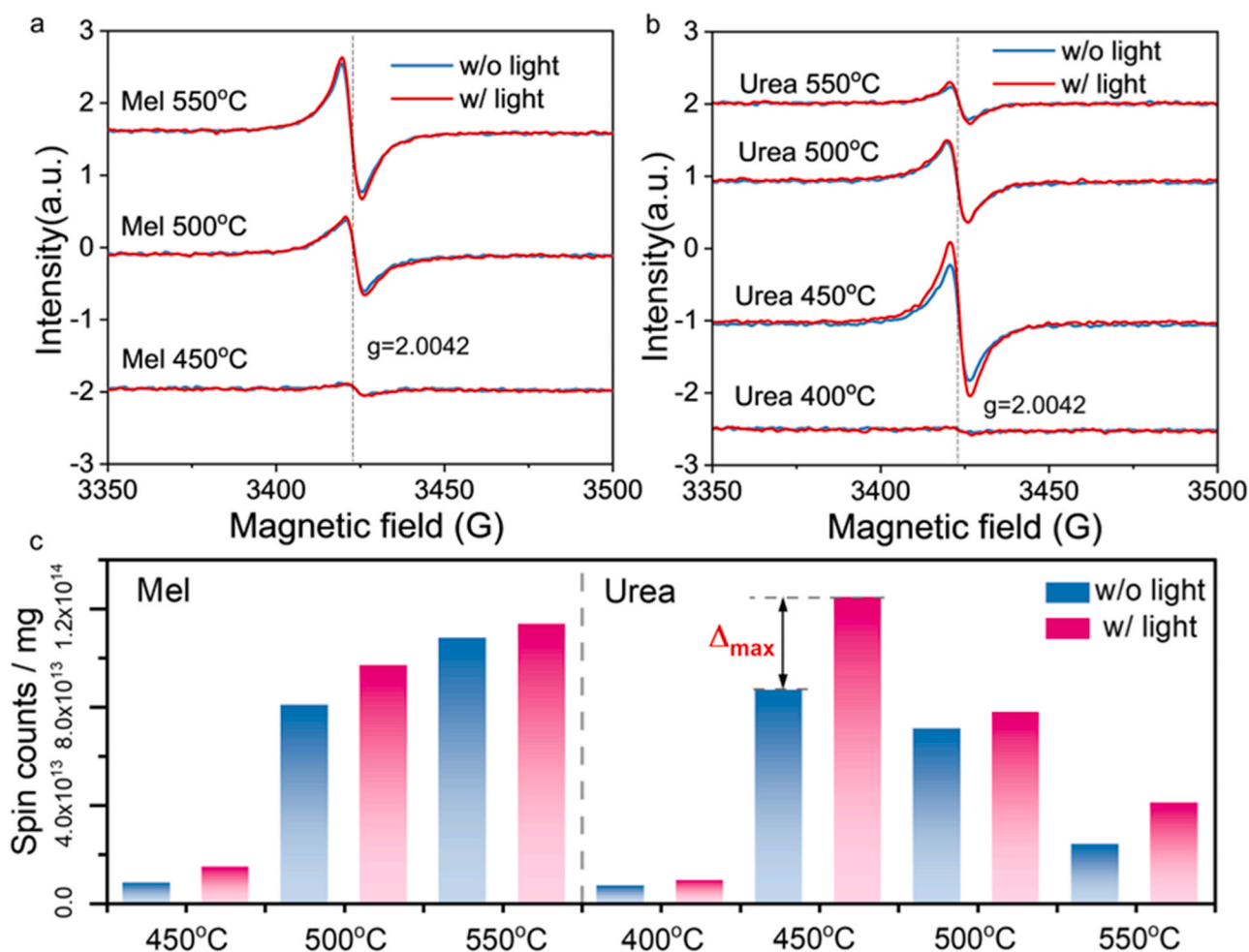

Fig. 3. Solid electron paramagnetic resonance (EPR) spectra of C_3N_4-Mel (a) and C_3N_4-Urea (b). Delocalization electron concentration (c) from EPR quantification results with (w/) and without (w/o) visible light.
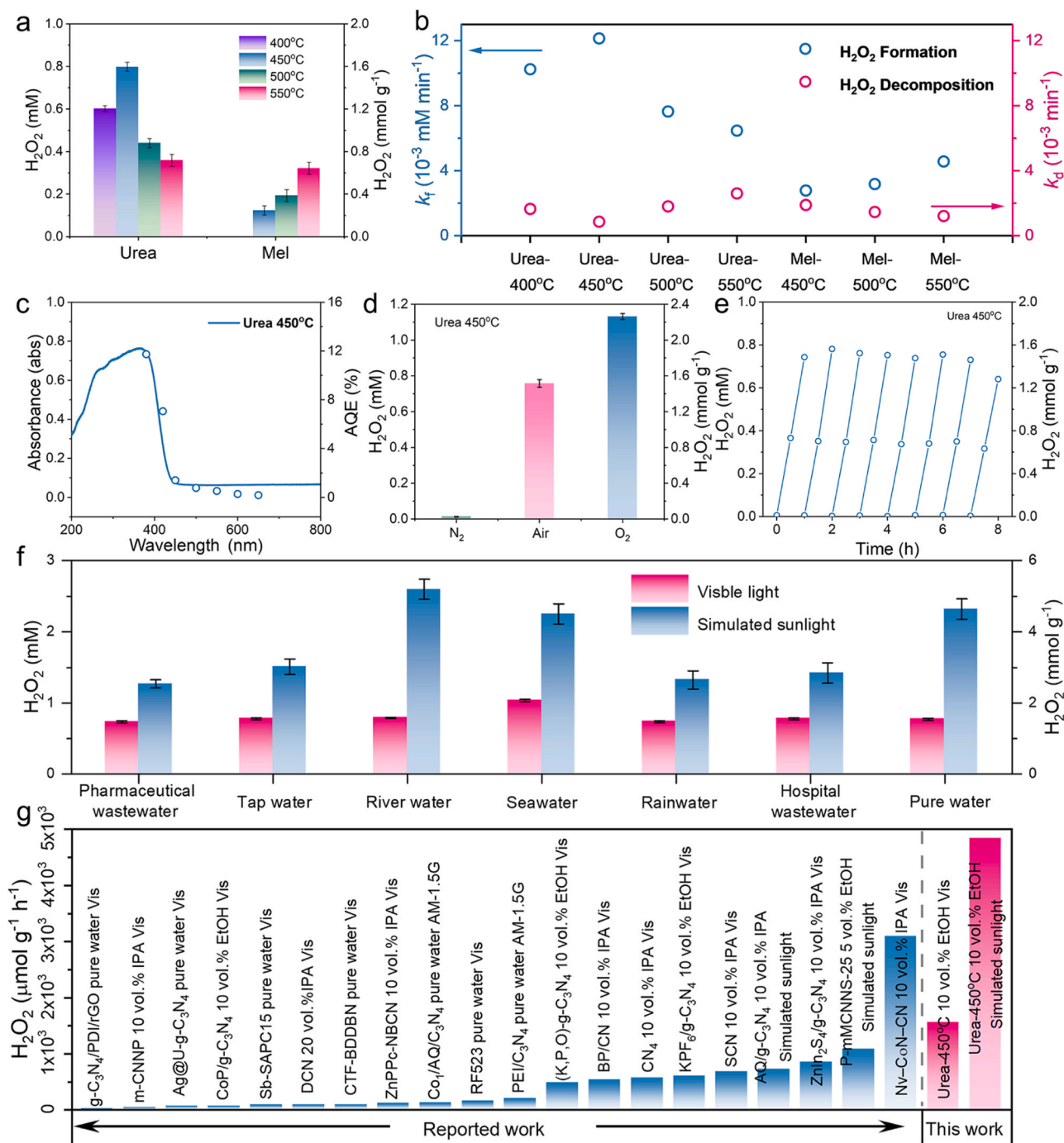
Fig. 4. Photocatalytic H_2O_2 production (a) by C_3N_4-Urea and C_3N_4-Mel. Experimental conditions: catalyst (0.5 g L^{-1}) with 10 vol% EtOH with Vis light ($\lambda \geq 400$ nm), T = 25 °C. Comparison (b) of the H_2O_2 formation rate constant (k_f, blue circle) with the H_2O_2 decomposition rate constant (k_d, red circle). AQE (c) of H_2O_2 production. Stability (d) of photocatalytic H_2O_2 production. Effect of dissolved oxygen (e) on H_2O_2 production in 1 h. Photocatalytic H_2O_2 production (f) over Urea 450 °C in different real water sample containing 10 vol% EtOH under Vis light ($\lambda \geq 400$ nm) and simulated sunlight·H_2O_2 production rates (g) for Urea 450 °C in this work compared with reported work.

times greater than Mel 550 °C. It is imperative to acknowledge that the yield of H_2O_2 hinges upon both the formation rate (k_f) and decomposition rate (k_d) (Fig. 4b). The kinetic equation can be summarized as $[H_2O_2] = (k_f/k_d) \{1-\exp(-k_d\ t)\}$, where k_f and k_d were obtained by assuming corresponding zero-order and first-order kinetics (Figs. S12 and S13). These results show that Urea 450 °C has the highest k_f and lowest k_d, suggesting a higher overall H_2O_2 yield than that in the other conditions.

The AQE of Urea 450 °C was calculated at selected wavelengths

(Fig. 4c). Urea 450 °C exhibited an AQE of H_2O_2 production close to 11.7%, 7.05%, 1.4%, 0.76%, 0.52%, 0.27% and 0.18% at wavelengths of 380, 420, 450, 500, 550, 600 and 650 nm, respectively. Overall, Urea 450 °C exhibited the high photocatalytic activity of H_2O_2 production and highest uptake of O_2, indicating the retarded charge recombination of delocalized electrons in Urea 450 °C with smaller sheet and few-layer. Moreover, the processes of H_2O_2 production over Urea 450 °C for different pH (pH 1–11) were also explored (Fig. S14), and the optimum pH is 1, demonstrating that the strong protonation environment favors

the photocatalytic H_2O_2 production of Urea 450 °C. Note that neither Urea 450 °C nor Mel 550 °C produced H_2 in the strong proton environment (pH = 1 and 3), suggesting that photogenerated electrons were used exclusively for H_2O_2 production and not for H_2 production (Fig. S15). The Zeta potential was further used to detect surface charge states at Urea 450 °C and Mel 550 °C. As shown in Fig. S16, a lower pH represents a higher Zeta potential, due to that high concentration of H^+ in the solution induces the more positive charge on the particle surface. Interestingly, the Zeta potential of Urea 450 °C is higher than Mel 550 °C, especially at pH= 1 and pH= 3, implying that the surface of Urea 450 °C has a stronger proton environment than that of Mel. To identify the role of O_2 in H_2O_2 production, different O_2/N_2 atmospheres were tested. As shown in Fig. 4d, the H_2O_2 yield is higher in the presence of O_2, suggesting an ORR mode for Urea 450 °C.

The realization of practical applications depends on a multitude of pivotal factors, encompassing robust stability, appropriate medium, and high activity. Notably, the yield achieved with the as-prepared Urea 450 °C catalyst exhibits remarkable stability over eight consecutive cycles (Fig. 4e). Moreover, the H_2O_2 yield in various real water samples and under distinct wavelength spectra is presented in Fig. 4f. It is noteworthy that the H_2O_2 yield attained in river water and pure water under simulated sunlight approaches approximately 5.4 and 4.9 mmol g^{-1} h^{-1}, respectively. A crucial observation is that this yield substantially surpasses that of most previously reported carbon nitride-based photocatalysts (Fig. 4g and Table S2), underscoring the superior performance of Urea 450 °C in the realm of H_2O_2 photosynthesis.

The electron transfer pathway was meticulously conducted through a comprehensive analysis utilizing a rotating ring-disk electrode (RRDE) at 1600 rpm in an O_2-saturated phosphate buffer solution (0.1 M, pH 7) [5,35]. The ORR polarization curves are displayed in Fig. 5a. Compare with Mel 550 °C, Urea 450 °C shows the higher onset potential (0.45 V vs. 0.41 V), and significant higher ring current (Fig. 5a). Particularly noteworthy is the exceptional H_2O_2 yield coupled with an impressive

98% selectivity, realized at 0.11 V (vs. RHE) in Urea 450 °C (Fig. 5b). Further analysis reveals that, in contrast to Mel 550 °C, Urea 450 °C exhibits approximately a two-electron (2e⁻) transfer mechanism (Fig. 5c) from 0.0 to 0.15 V (vs. RHE). These results show the outstanding 2e⁻ ORR capabilities of Urea 450 °C with abundant delocalized electrons for H_2O_2 production with high efficiency and selectivity.

In the ORR to produce H_2O_2 production, the initial step involves O_2 adsorption onto the catalyst surface. The O_2 temperature-programmed desorption (O_2-TPD) curve reveals that Urea 450 °C has a higher O_2 adsorption (0.26 mmol g^{-1}) than Mel 550 °C (0.08 mmol g^{-1}) (Fig. 6a). To delve into the intricate details of the intermediates generated during the photocatalytic H_2O_2 production mediated by Urea 450 °C, EPR experiments were employed to unveil the reactive species [36,37]. Notably, as depicted in Fig. 6b and S17, *O_2 signal of Urea 450 °C gradually intensified over time, ultimately reaching a level 2.27 times higher than that of Mel 550 °C, indicating that Urea 450 °C exhibits a greater propensity than Mel 550 °C for electron loss during the ORR. To further reveal the reaction mechanism, different sacrificial agents were added to initial solution (Fig. S18), showing superoxide (*O_2^-) as the main active specie for H_2O_2 production [38].

To reveal carriers migration of Urea 450 °C, the transient photo current response is depicted in Fig. 6c, manifesting obvious and repeatable photo current signals with on/off of applying visible light. The current intensity of Urea 450 °C is significantly higher than that of Mel 550 °C. The Urea 450 °C displays the higher migration rate of carriers, and the result is matched well with H_2O_2 production. Electrochemical impedance spectroscopy (EIS) further explains a high-efficient carriers transfer of Urea 450 °C (Fig. 6d). The arc diameter of Urea 450 °C is the smaller than that of Mel 550 °C. The smaller diameter is due to the lower charge transfer resistance and the faster mobility of electrons [39–41]. Equivalent circuit diagram was used to fit EIS data. and R_s, R_{ct}, Q and Z_w represent the resistance of the solution, the charge transfer resistance value between the electrode and solution, the
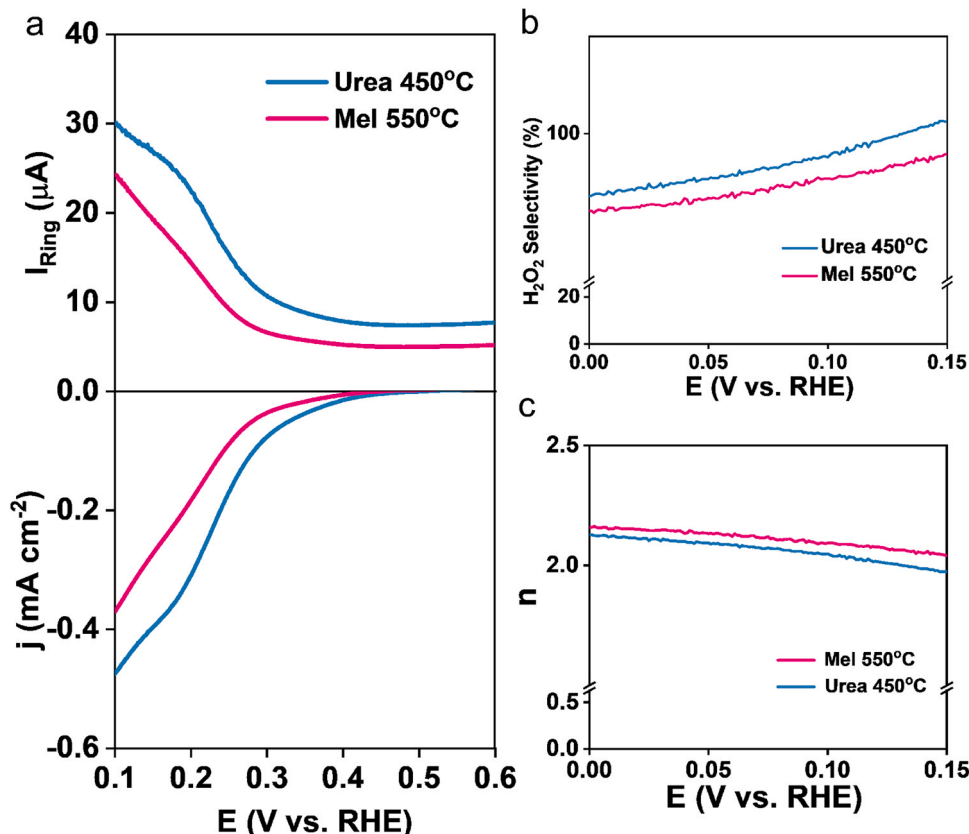

Fig. 5. ORR polarization curves (a), H_2O_2 selectivity (b) and the corresponding number (c) of transferred electrons of electrochemical H_2O_2 production.
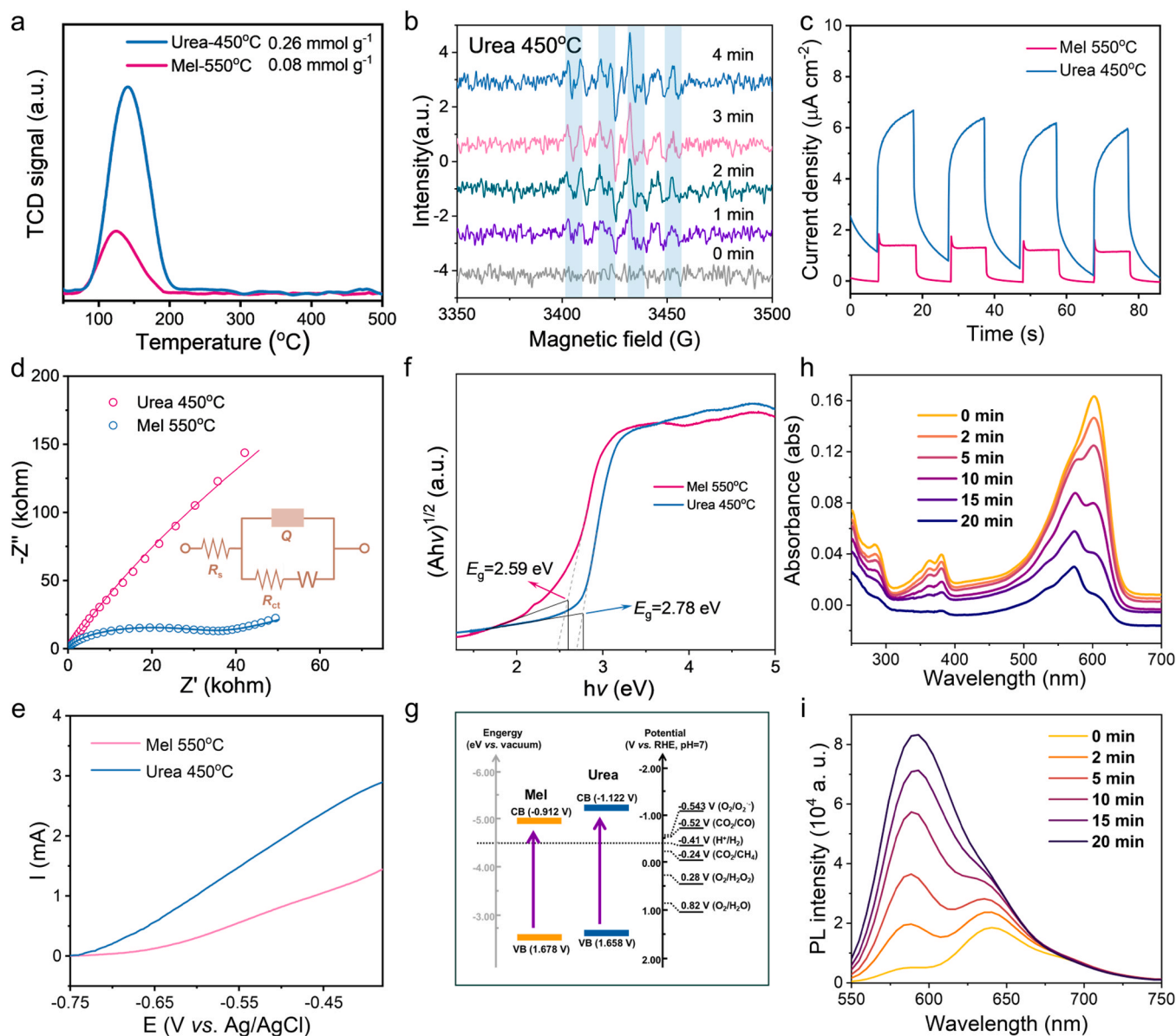
Fig. 6. O_2-TPD curves (a), EPR detection of DMPO-*O_2^- (b), photocurrent (c), LSV (d), Nyquist plots and Equivalent circuit by simulating EIS (e), Tauc plots (f) and energy band structures (g) of Mel 550 °C and Urea 450 °C. Real-time UV–Vis absorption (h) and fluorescence spectra (i) of the reductive reaction from resazurin to resorufin for Urea 450 °C under visible light.

electrode double-layer capacitance and Warburg impedance, respectively. The simulated R_{ct} values are shown in Table S3. These indicate that more delocalized electrons contribute to higher charges transfer efficiency of Urea 450 °C. The faster charge transfer allows to drive electrochemical reactions. As shown in Fig. 6e, relative to the Mel 550 °C, linear sweep voltammograms (LSV) curve of Urea 450 °C exhibits a higher current response from −0.75 to −0.4 V. These results fully demonstrate that abundant delocalized electrons of Urea 450 °C can rapidly improve the separation rate of carriers [42,43]. To probe the charge migration behaviors, the energy band structure of all samples was evaluated through the by Tauc plots and Mott-Schottky plots (Fig. 6f, S19 and S20). In contrast to Mel 550 °C, Urea 450 °C exhibits an easier photoexcitation performance, and a more negative reduction potential for easier photocatalytic ORR activity (Fig. 6g). These fully confirm that Urea 450 °C has excellent visible light utilization ability and the prospect of photocatalytic H_2O_2 production.

To visually demonstrate the effective reductive reaction on Urea 450 °C, we conducted an electron reductive reaction (ERR) study using a standard reductive probe molecule, resazurin [44]. The reductive reaction scheme and photographs illustrating resazurin's transformation are presented in Figs. S21 and S22. Once the system reached an equilibrium adsorption state, the photoreaction of resazurin was monitored by real-time UV–Vis absorption and fluorescence emission (with an excitation wavelength of 532 nm) under visible light (Fig. 6h and i). These results reveal a noticeable decrease in peak intensity at 602 nm with increasing light irradiation time, indicating the transformation of resazurin into resorufin due to the influence of photogenerated electrons. Particularly noteworthy was the distinct increase in fluorescence emission at 580 nm as the light irradiation progressed. After light irradiation for 20 min, the intensity of fluorescence emission around 580 nm increased by 15.7 times (Fig. 6i). These findings collectively underscore the significant role played by the abundant delocalized electrons in Urea 450 °C, effectively suppressing the recombination of photogenerated electron-hole pairs.

To further understand the charge carrier behavior of Mel 550 °C and Urea 450 °C, single-particle PL spectra were explored (Fig. 7). Single-
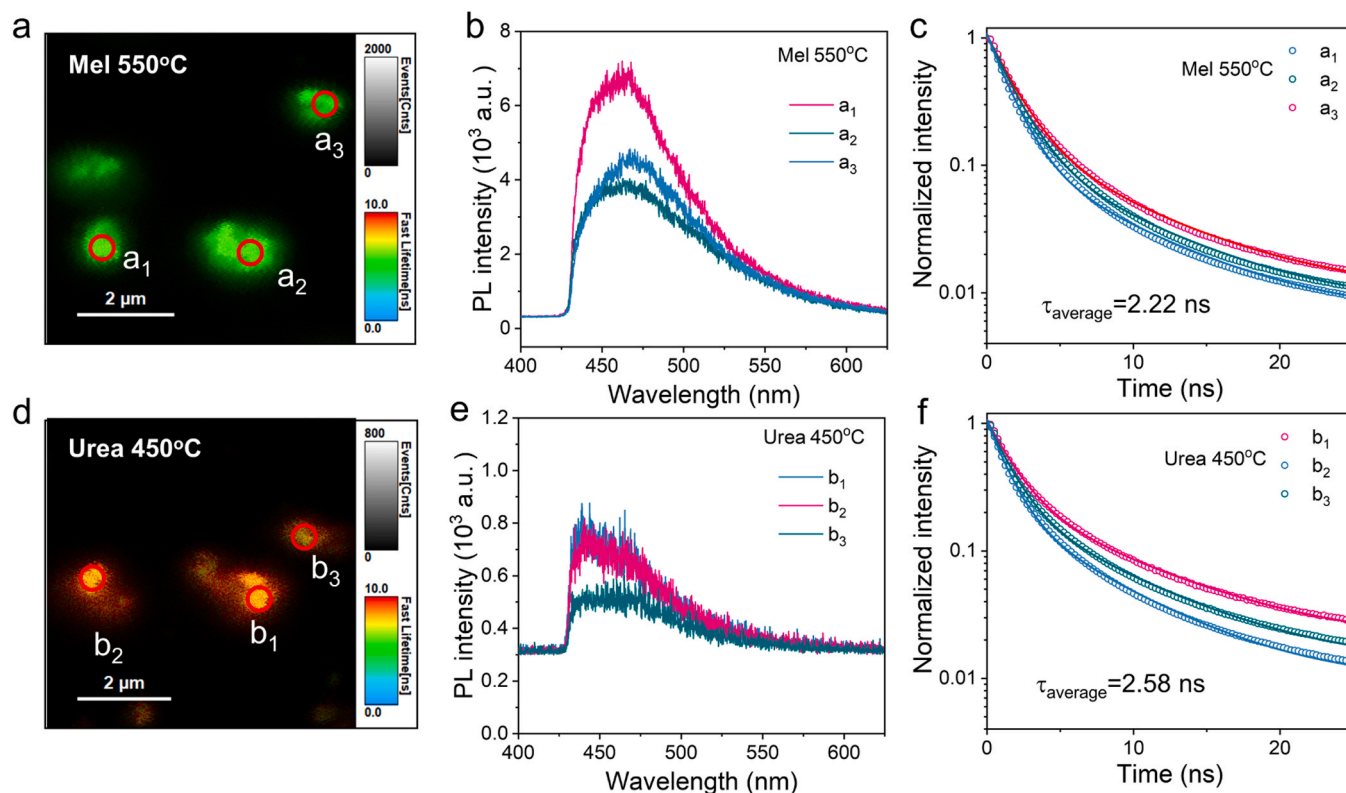
Fig. 7. Low-magnification dark-field micrographs (a and d), single-particle PL spectra (b and e), time-resolved PL spectra (c and f) of Mel 550 °C and Urea 450 °C.

particle PL microscope with a picosecond laser at a wavelength of 405 nm was used to demonstrate time-resolved photogenerated electron formation with an electron multiplying charge-coupled device (EMCCD) camera (Fig. S23). A single-particle PL image of Mel 550 °C (Fig. 7a) displays three bright points, while that of Urea 450 °C shows the decreased brightness (Fig. 7d), implying PL quenching. Single-particle PL spectra of Mel 550 °C (Fig. 7b) corresponding to a_1, a_2, and a_3 points in Fig. 7a exhibit a similar shape and a strong signal around 470 nm. In contrast to Mel 550 °C, three particles of Urea 450 °C show much weaker PL signal (Fig. 7e) around 445 nm, demonstrating PL quenching. Average PL quenching efficiency is calculated to be 86.5% for Urea 450 °C, relative to Mel 550 °C. Time-resolved PL spectra on all particles of two samples are shown in Fig. 7c and f. The PL decay curve for Mel 550 °C, and Urea 450 °C were fitted by double exponential functions, and results with a short electron lifetime (τ_{AV1}) = 1.53 ns (87%) and a long electron lifetime (τ_{AV2}) = 6.79 ns (13%) for Mel 550 °C and with τ_{AV1} = 1.43 ns (79%) and τ_{AV2} = 6.76 ns (21%) for Urea 450 °C were observed. Detailed τ_1 and τ_2 on all particles are fitted in Table S4. The short and long lifetimes are always attributed to electrons trapped at shallow and deep sites prior to charge recombination. Urea 450 °C has longer lifetimes than Mel 550 °C, suggesting that large number of delocalized electrons in Urea 450 °C act as electrons trap sites [45], and photogenerated electrons are rapidly transferred via delocalized electrons to surface reaction sites in Urea 450 °C.

To understand deeper the role of surface charge, the surface potential distribution of both Mel 550 °C and Urea 450 °C was explored by KPFM (Fig. 8a, b and S24) [46]. For Urea 450 °C, the contact potential difference (CPD) spanned a range of approximately 460~490 mV, conspicuously higher than the 280~310 mV range observed for Mel 550 °C. Notably, Urea 450 °C exhibited an significant increase of average surface potential of ≈ 35.7 mV with light, relative to its non-illuminated state (Fig. 8d), while Mel 550 °C demonstrated a smaller increase of ≈ 9.07 mV under light irradiation (Fig. 8c). This phenomenon can be attributed to the amplification of directional charge

transfer induced by abundant delocalized electrons in Urea 450 °C upon light exposure.

To further verify the antibacterial efficiency of photocatalytic H_2O_2 production by Urea 450° on water disinfection, we evaluated the antibacterial performance of Urea 450 °C against gram-positive MRSA in a co-culture setup (Fig. 9). As shown in Fig. 9a, the antibacterial effect of H_2O_2 production enhanced with the increasing of irradiation time, and the H_2O_2 production at 60 min emerged the strongest inhibitory antibacterial effect with barely growing. Furthermore, we explored the antibacterial mechanism of Urea 450 °C against MRSA. Firstly, MRSA treated with Urea 450 °C by irradiation for 0, 20, 40 and 60 min were stained by the SYTO9 and propidium iodide (PI) fluorescence for distinguishing the live and dead bacteria (Fig. 9b and S25). As expected, strong green and negligible red fluorescence were observed at 0 min, while the green fluorescence was decreased, and red fluorescence was increased with the extension of processing time. In addition, the protein leakage increased in dose-dependent manner after Urea 450 °C treatment by irradiation for 0, 20, 40 and 60 min (Fig. 9c). A series of experiments was carried out to explore oxidative stress, including ATP intensity, protein and lipid oxidation detection (Fig. 9d-f). We found that the ATP intensity significantly reduced with the increasing of irradiation time. On the contrary, the levels of MDA and PCA significantly enhanced with the increase of H_2O_2 concentrations, indicating that H_2O_2 induced cell membrane damage by lipid and protein oxidization, and damaged mitochondrial function, leading to ultimately bacterial inactivation. These observations demonstrated that H_2O_2 generation by Urea 450 °C with abundant delocalized electrons can induce bacterial inactivation for efficiently bactericidal for water disinfection.

To evaluate the potential application of in-situ self-photo-Fenton in antibiotic wastewater, a continuous flow reaction system (Fig. 10a) was used to treat OTC and its ARGs [47]. As shown in Fig. 10b, the OTC concentration rapidly decayed by 3.75 min^{-1}, which was completely transformed within 2 min, demonstrating the efficient antibiotic removal capability. The mechanisms of OTC antibiotic resistance in
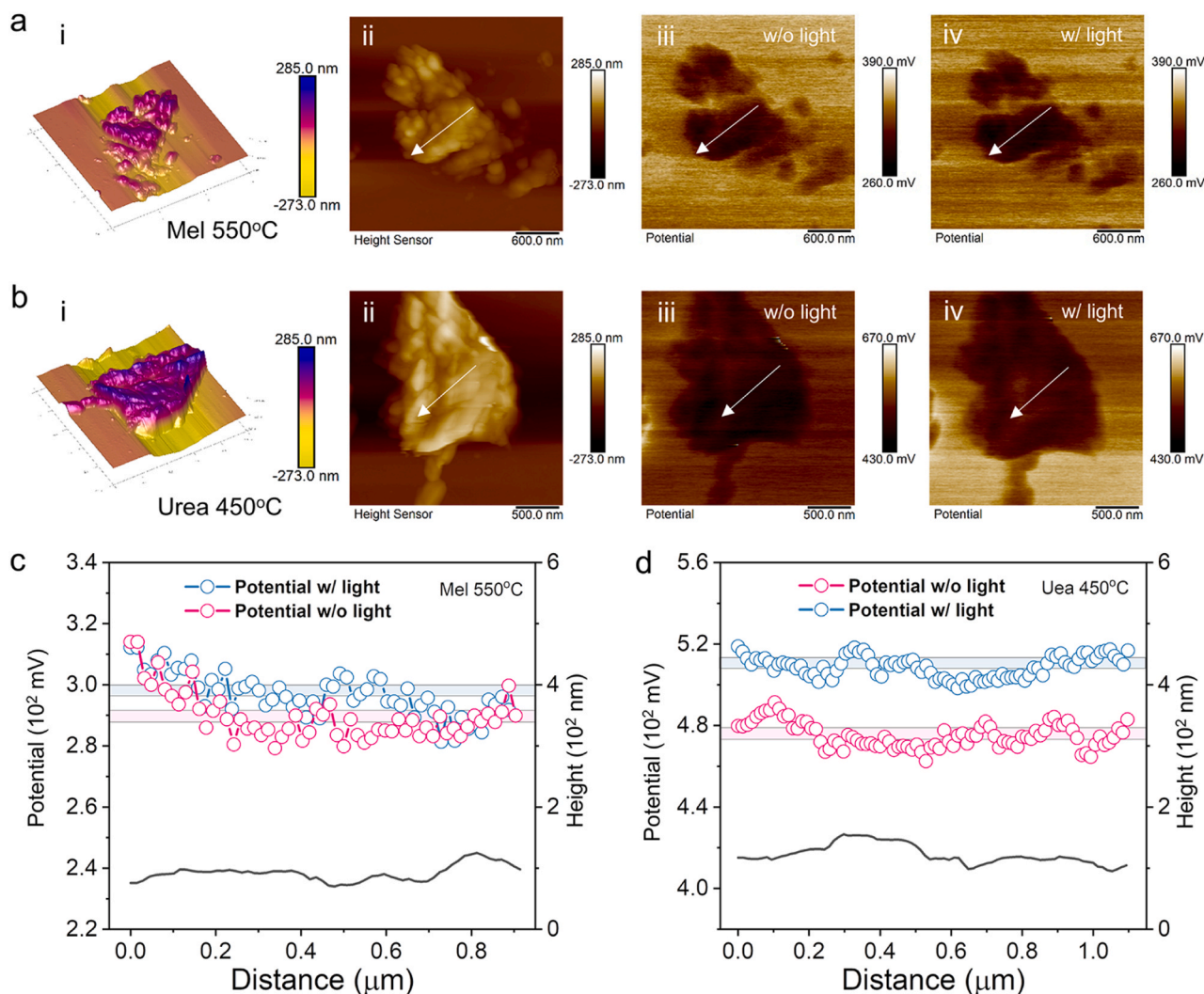
Fig. 8. Surface morphologies and corresponding KPFM potential images of Mel 550 °C (a) and Urea 450 °C (b). i, AFM 3D topography images. ii, AFM 2D topography images. iii, iv, contact potential difference (CPD) of Mel 550 °C/Urea 450 °C with and without light. The arrow is the selected surface potential area. Surface potential from KPFM images (c and d) of Mel 550 °C and Urea 450 °C w/ and w/o light irradiation.

bacteria include efflux pump, modification antibiotic target and enzyme modification [48]. In this study, 9 dominant OTC ARGs were amplified and 16 s RNA was applied as its reference gene. As shown in Fig. 10c, efflux pump ARGs (*tetA* 4.47×10^{-4}, *tetC* 8.01×10^{-4} and *tetG* 4.43×10^{-4}) were the most dominant ARGs, followed by enzyme modification ARGs (*tetX* 4.44×10^{-4}) and ribosome site modification ARGs (*tetM* 2.76×10^{-4}). Moreover, agarose gel electrophoresis was used to verify the purity of gained ARGs for subsequent degradation (Fig. 10d). The dominant ARGs subtypes of *tetC*, *tetM* and *tetX* were also insufficiently removed in 60 min (Fig. 10e, S26 and S27). After 40 min of treatment, the disappearance of bands treated by in-situ self-photo-Fenton system suggests that *tetC* are not capable of amplification. All the above results demonstrated that the inactivation of antibiotics and the degradation of ARGs could be achieved simultaneously by the in-situ self-photo-Fenton system with Urea 450 °C, which is expected to be expanded into practical applications.

4. Conclusion

In summary, we report two precursors of carbon nitride with urea and Mel. Compare with C_3N_4-Mel, C_3N_4-Urea exhibits superior H_2O_2 photosynthesis activity. Such a high performance was attributed to that C_3N_4-Urea activate more delocalized electrons due to its smaller size and

thickness, inducing more exposed sites for electron delocalization stemming from π-π stacking interactions. These exposed delocalized electrons are used as electronic bridges and active sites to facilitate the directional transfer of photogenerated carriers. Meanwhile, O_2 is easily trapped on the surface of C_3N_4-Urea, owning to the large specific surface area, leading to a rapid H_2O_2 production process via an indirect 2e⁻ reduction pathway. In addition, the in-situ self-photo-Fenton system was also constructed, demonstrating efficient disinfection ability, antibiotic and its ARGs removal ability. This kind of molecular engineering induces abundant delocalized electrons to boost the separation of photogenerated carriers and offers a reliable strategy for the design of catalytic materials for energy conversion and environmental remediation.

CRediT authorship contribution statement

Zhu Mingshan: Conceptualization, Funding acquisition, Supervision, Writing – review & editing. **Yun Yang:** Funding acquisition, Supervision, Writing – review & editing. **Zhai Chunyang:** Formal analysis, Investigation, Methodology. **He Yupeng:** Formal analysis, Investigation, Methodology. **Tong Kangbo:** Formal analysis, Investigation, Methodology. **Lv Hao:** Formal analysis, Investigation, Methodology. **Li Zhi:** Conceptualization, Data curation, Formal analysis, Investigation,
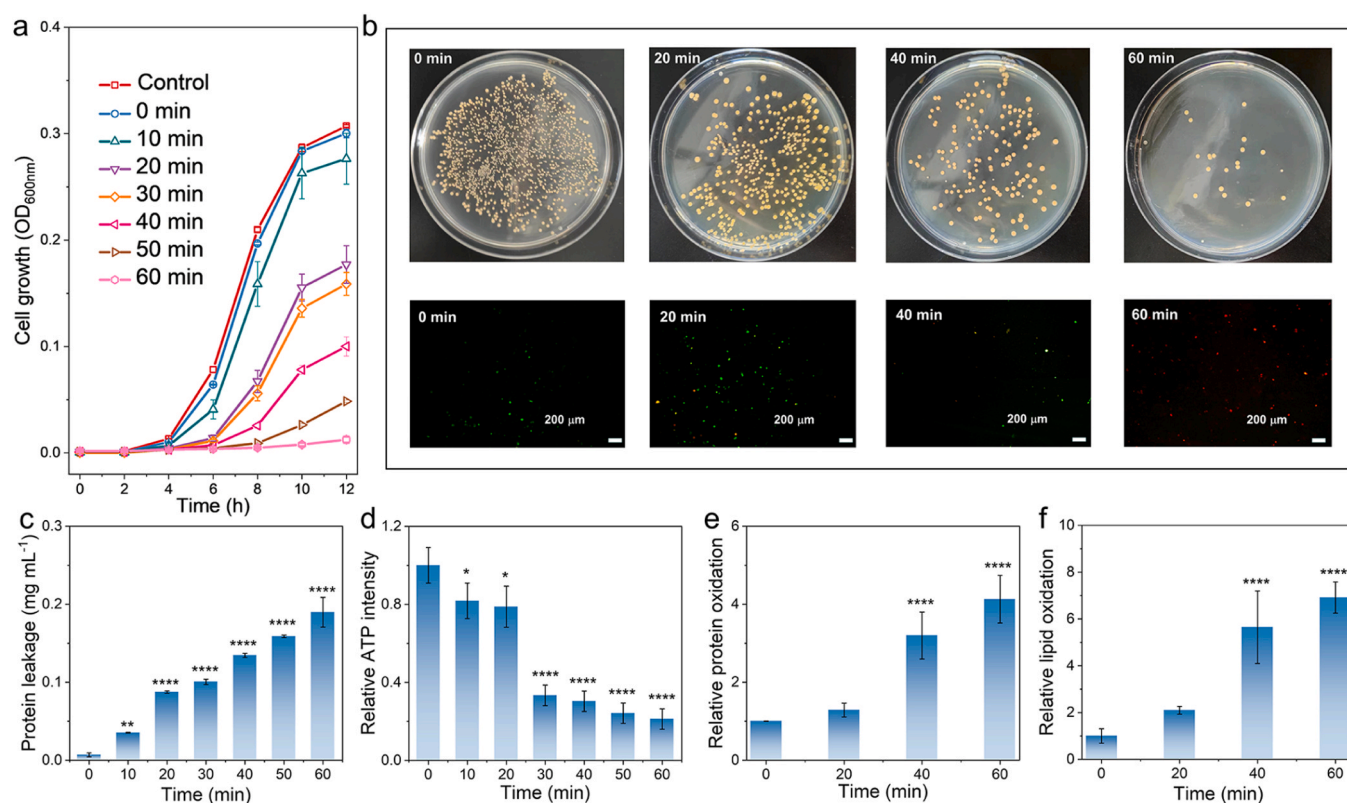
Fig. 9. MRSA growth curves (a), plate incubated with LB medium and live/dead staining (merge) (b), protein leakage (c), relative ATP intensities (d), relative protein oxidation (e), and relative lipid oxidation (f) of Urea 450 °C at different time. *($P < 0.05$); **($P < 0.01$); ***($P < 0.001$); **** ($P < 0.0001$) (Scale bar = 200 μm).
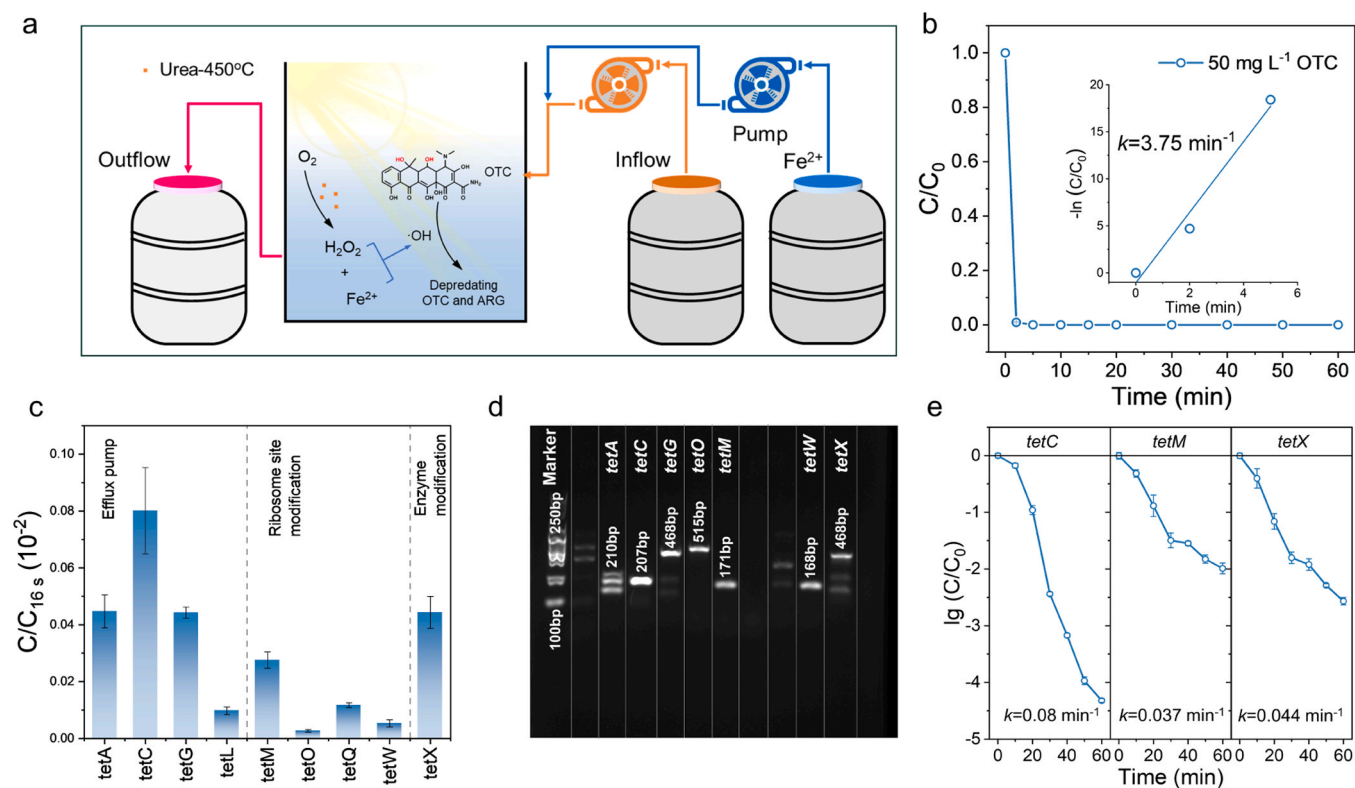

Fig. 10. Schematic diagram of the continuous-flow reactor (a). Degradation efficiencies of OTC (b). The proportion of 3 typical ARGs produced by OTC (c), including efflux pump (*tetA*, *tetC*, *tetG*, and *tetL*), ribosome site modification (*tetO*, *tetM*, *tetQ*, and *tetW*), enzyme modification (*tetX*). Agarose gel electrophoresis of ARGs (d). Degradation time profiles (e) of *tetC*, *tetM*, and *tetX*.

Methodology, Writing – original draft.

Declaration of Competing Interest

The authors declare that they have no known competing financial interests or personal relationships that could have appeared to influence the work reported in this paper.

Data Availability

Data will be made available on request.

Acknowledgements

Appendix A. Supporting information

Supplementary data associated with this article can be found in the online version at doi:10.1016/j.apcatb.2024.123690.

References

[1] C. Xia, Y. Xia, P. Zhu, L. Fan, H. Wang, Direct electrosynthesis of pure aqueous H_2O_2 solutions up to 20% by weight using a solid electrolyte, Science 366 (2019) 226–231.

[2] Z. Li, Y. Li, S. Chen, Q. Zha, M. Zhu, In-situ monitoring of hydrogen peroxide production at nickel single-atom electrocatalyst, Chem. Eng. J. 460 (2023) 141657.

[3] S. Chen, T. Luo, X. Li, K. Chen, J. Fu, K. Liu, C. Cai, Q. Wang, H. Li, Y. Chen, C. Ma, L. Zhu, Y. Lu, T. Chan, M. Zhu, E. Cortés, M. Liu, Identification of the highly active Co–N_4 coordination motif for selective oxygen reduction to hydrogen peroxide, J. Am. Chem. Soc. 144 (2022) 14505–14516.

[4] Y. Zhang, C. Pan, G. Bian, J. Xu, Y. Dong, Y. Zhang, Y. Lou, W. Liu, Y. Zhu, H_2O_2 generation from O_2 and H_2O on a near-infrared absorbing porphyrin supramolecular photocatalyst, Nat. Energy 8 (2023) 361–371.

[5] Y.-X. Ye, J. Pan, F. Xie, L. Gong, S. Huang, Z. Ke, F. Zhu, J. Xu, G. Ouyang, Highly efficient photosynthesis of hydrogen peroxide in ambient conditions, Proc. Natl. Acad. Sci. U. S. A. 118 (2021) e2103964118.

[6] Z. Li, Y. Zhou, Y. Zhou, K. Wang, Y. Yun, S. Chen, W. Jiao, L. Chen, B. Zou, M. Zhu, Dipole field in nitrogen-enriched carbon nitride with external forces to boost the artificial photosynthesis of hydrogen peroxide, Nat. Commun. 14 (2023) 5742.

[7] C. Pan, G. Bian, Y. Zhang, Y. Lou, Y. Zhang, Y. Dong, J. Xu, Y. Zhu, Efficient and stable H_2O_2 production from H_2O and O_2 on $BiPO_4$ photocatalyst, Appl. Catal. B: Environ. 316 (2022) 121675.

[8] Z. Wei, S. Zhao, W. Li, X. Zhao, C. Chen, D.L. Phillips, Y. Zhu, W. Choi, Artificial photosynthesis of H_2O_2 through reversible photoredox transformation between catechol and o-benzoquinone on polydopamine-coated CdS, ACS Catal. 12 (2022) 11436–11443.

[9] Z. Wei, W. Li, J. Hu, X. Ma, Y. Zhu, Interfacial internal electric field and oxygen vacancies synergically enhance photocatalytic performance of bismuth oxychloride, J. Hazard. Mater. 402 (2021) 123470.

[10] X. Wang, H. Jiang, M. Zhu, X. Shi, Cascaded electron transition proved by femto-second transient absorption spectroscopy for enhanced photocatalysis hydrogen generation, Chin. Chem. Lett. 34 (2023) 107683.

[11] C. Liu, J. Zhang, W. Wang, L. Chen, M. Zhu, Progress in the synthesis and applications of N-rich carbon nitride (C_3N_5)-based catalysts in environmental and energy catalysis, Surf. Interfaces 42 (2023) 103491.

[12] J. He, X. Wang, S. Jin, Z.-Q. Liu, M. Zhu, 2D metal-free heterostructure of covalent triazine framework/g-C_3N_4 for enhanced photocatalytic CO_2 reduction with high selectivity, Chin. J. Catal. 43 (2022) 1306–1315.

[13] L. Jian, Y. Dong, H. Zhao, C. Pan, G. Wang, Y. Zhu, Highly crystalline carbon nitrogen polymer with a strong built-in electric fields for ultra-high photocatalytic H_2O_2 production, Appl. Catal. B: Environ. (2023) 123340.

[14] W. Li, Z. Wei, K. Zhu, W. Wei, J. Yang, J. Jing, D.L. Phillips, Y. Zhu, Nitrogen-defect induced trap states steering electron-hole migration in graphite carbon nitride, Appl. Catal. B: Environ. 306 (2022) 121142.

[15] Y.-N. Liu, C.-C. Shen, N. Jiang, Z.-W. Zhao, X. Zhou, S.-J. Zhao, A.-W. Xu, g-C_3N_4 hydrogen-bonding viologen for significantly enhanced visible-light photocatalytic H_2 evolution, ACS Catal. 7 (2017) 8228–8234.

[16] W. Li, Z. Wei, Y. Sheng, J. Xu, Y. Ren, J. Jing, J. Yang, J. Li, Y. Zhu, Dual cocatalysts synergistically promote perylene diimide polymer charge transfer for enhanced photocatalytic water oxidation, ACS Energy Lett. 8 (2023) 2652–2660.

[17] H. Liu, H. Li, J. Lu, S. Zeng, M. Wang, N. Luo, S. Xu, F. Wang, Photocatalytic cleavage of C–C bond in lignin models under visible light on mesoporous graphitic carbon nitride through π–π stacking interaction, ACS Catal. 8 (2018) 4761–4771.

[18] X. Zhang, P. Ma, C. Wang, L. Gan, X. Chen, P. Zhang, Y. Wang, H. Li, L. Wang, X. Zhou, K. Zheng, Unraveling the dual defect sites in graphite carbon nitride for ultra-high photocatalytic H_2O_2 evolution, Energy Environ. Sci. 15 (2022) 830–842.

[19] Y.-P. Zhu, T.-Z. Ren, Z.-Y. Yuan, Mesoporous phosphorus-doped g-C_3N_4 nanostructured flowers with superior photocatalytic hydrogen evolution performance, ACS Appl. Mater. Interfaces 7 (2015) 16850–16856.

[20] H. Dong, X. Guo, C. Yang, Z. Ouyang, Synthesis of g-C_3N_4 by different precursors under burning explosion effect and its photocatalytic degradation for tylosin, Appl. Catal. B: Environ. 230 (2018) 65–76.

[21] S. Cao, J. Low, J. Yu, M. Jaroniec, Polymeric photocatalysts based on graphitic carbon nitride, Adv. Mater. 27 (2015) 2150–2176.

[22] F. Dong, Z. Wang, Y. Sun, W.-K. Ho, H. Zhang, Engineering the nanoarchitecture and texture of polymeric carbon nitride semiconductor for enhanced visible light photocatalytic activity, J. Colloid Interf. Sci. 401 (2013) 70–79.

[23] C. Guan, J. Jiang, S. Pang, X. Chen, R.D. Webster, T.-T. Lim, Facile synthesis of pure g-C_3N_4 materials for peroxymonosulfate activation to degrade bisphenol A: Effects of precursors and annealing ambience on catalytic oxidation, Chem. Eng. J. 387 (2020) 123726.

[24] S. Dyjak, W. Kiciński, A. Huczko, Thermite-driven melamine condensation to $C_xN_yH_z$ graphitic ternary polymers: towards an instant, large-scale synthesis of gC_3N_4, J. Mater. Chem. A 3 (2015) 9621–9631.

[25] W. Yan, L. Yan, C. Jing, Impact of doped metals on urea-derived g-C_3N_4 for photocatalytic degradation of antibiotics: Structure, photoactivity and degradation mechanisms, Appl. Catal. B: Environ. 244 (2019) 475–485.

[26] C. Shao, Q. He, M. Zhang, L. Jia, Y. Ji, Y. Hu, Y. Li, W. Huang, Y. Li, A covalent organic framework inspired by C_3N_4 for photosynthesis of hydrogen peroxide with high quantum efficiency, Chin. J. Catal. 46 (2023) 28–35.

[27] S. Lan, X. Ke, Z. Li, L. Mai, M. Zhu, E.Y. Zeng, Piezoelectric disinfection of water co-polluted by bacteria and microplastics energized by water flow, ACS EST Water 2 (2022) 367–375.

[28] J. Zhang, Z. Li, J. He, H. Tao, M. Chen, Y. Zhou, M. Zhu, Reinforced photogenerated electrons in few-layer C_3N_5 for enhanced catalytic NO oxidation and CO_2 reduction, ACS Catal. 13 (2022) 785–795.

[29] G.P. Mane, S.N. Talapaneni, K.S. Lakhi, H. Ilbeygi, U. Ravon, K. Al-Bahily, T. Mori, D.H. Park, A. Vinu, Highly ordered nitrogen-rich mesoporous carbon nitrides and their superior performance for sensing and photocatalytic hydrogen generation, Angew. Chem. Int. Ed. 56 (2017) 8481–8485.

[30] J. Zhang, B. Jing, Z. Tang, Z. Ao, D. Xia, M. Zhu, S. Wang, Experimental and DFT insights into the visible-light driving metal-free C_3N_5 activated persulfate system for efficient water purification, Appl. Catal. B: Environ. 289 (2021) 120023.

[31] S.N. Talapaneni, G.P. Mane, A. Mano, C. Anand, D.S. Dhawale, T. Mori, A. Vinu, Synthesis of nitrogen-rich mesoporous carbon nitride with tunable pores, band gaps and nitrogen content from a single aminoguanidine precursor, ChemSusChem 5 (2012) 700–708.

[32] P. Zhang, Y. Tong, Y. Liu, J.J.M. Vequizo, H. Sun, C. Yang, A. Yamakata, F. Fan, W. Lin, X. Wang, W. Choi, Heteroatom dopants promote two-electron O_2 reduction for photocatalytic production of H_2O_2 on polymeric carbon nitride, Angew. Chem. Int. Ed. 59 (2020) 16209–16217.

[33] K.S.W. Sing, Reporting physisorption data for gas/solid systems with special reference to the determination of surface area and porosity, Pure Appl. Chem. 57 (1985) 603–619.

[34] D. Zhao, C.L. Dong, B. Wang, C. Chen, Y.C. Huang, Z. Diao, S. Li, L. Guo, S. Shen, Synergy of dopants and defects in graphitic carbon nitride with exceptionally modulated band structures for efficient photocatalytic oxygen evolution, Adv. Mater. 31 (2019) 1903545.

[35] Q. Wu, J. Cao, X. Wang, Y. Liu, Y. Zhao, H. Wang, Y. Liu, H. Huang, F. Liao, M. Shao, Z. Kang, A metal-free photocatalyst for highly efficient hydrogen peroxide photoproduction in real seawater, Nat. Commun. 12 (2021) 483.

[36] C. Wu, G. Yu, Y. Yin, Y. Wang, L. Chen, Q. Han, J. Tang, B. Wang, Mesoporous polymeric cyanamide-triazole-heptazine photocatalysts for highly-efficient water splitting, Small 16 (2020) 2003162..

[37] J. He, Z. Yi, Q. Chen, Z. Li, J. Hu, M. Zhu, Harvesting mechanical energy induces piezoelectric polarization of MIL-100 (Fe) for cocatalyst-free hydrogen production, Chem. Commun. 58 (2022) 10723–10726.

[38] Z. Li, S. Lan, M. Zhu, Piezoelectricity activates persulfate for water treatment: a perspective, Environ. Sci. Ecotechnol. 18 (2024) 100329.

[39] Z. Li, Y. Xiao, F. Lai, X. Yan, D. You, K. Li, L. Zeng, M. Zhu, G. Xiao, J. Albert, T. Guo, Operando optical fiber monitoring of nanoscale and fast temperature changes during photo-electrocatalytic reactions, Light Sci. Appl. 11 (2022) 220.

[40] A.-Y. Zha, Q.-B. Zha, Z. Li, H.-M. Zhang, X.-F. Ma, W. Xie, M.-S. Zhu, Surfactant-enhanced electrochemical detection of bisphenol A based on Au on ZnO/reduced graphene oxide sensor, Rare Met. 42 (2023) 1274–1282.

[41] S. Wang, F. Chen, Z. Li, H. Tao, L. Qu, J. Li, M. Zhu, Q. Zha, A graphene oxide/Zn-metal organic framework electrochemical sensor for acetaminophen detection, Surf, Interfaces 39 (2023) 102910.

[42] T. Jia, L. Wang, Z. Zhu, B. Zhao, Y. Zhou, G. Zhu, M. Zhu, H. Tao, Modulating the degree of O vacancy defects to achieve selective control of electrochemical CO_2 reduction products, Chin. Chem. Lett. (2023) 108692.

[43] C. Dong, Y. Yang, X. Hu, Y. Cho, G. Jang, Y. Ao, L. Wang, J. Shen, J.H. Park, K. Zhang, Self-cycled photo-Fenton-like system based on an artificial leaf with a solar-to-H_2O_2 conversion efficiency of 1.46%, Nat. Commun. 13 (2022) 4982.

[44] J.B. Sambur, T.-Y. Chen, E. Choudhary, G. Chen, E.J. Nissen, E.M. Thomas, N. Zou, P. Chen, Sub-particle reaction and photocurrent mapping to optimize catalyst-modified photoanodes, Nature 530 (2016) 77–80.

[45] M. Zhu, S. Kim, L. Mao, M. Fujitsuka, J. Zhang, X. Wang, T. Majima, Metal-free photocatalyst for H_2 evolution in visible to near-infrared region: black phosphorus/graphitic carbon nitride, J. Am. Chem. Soc. 139 (2017) 13234–13242.

[46] R. Chen, F. Fan, T. Dittrich, C. Li, Imaging photogenerated charge carriers on surfaces and interfaces of photocatalysts with surface photovoltage microscopy, Chem. Soc. Rev. 47 (2018) 8238–8262.

[47] C. Zhai, Y. Chen, X. Huang, A.B. Isaev, M. Zhu, Recent progress on single-atom catalysts in advanced oxidation processes for water treatment, Environ. Funct. Mater. 1 (2022) 219–229.

[48] E.M. Darby, E. Trampari, P. Siasat, M.S. Gaya, I. Alav, M.A. Webber, J.M. Blair, Molecular mechanisms of antibiotic resistance revisited, Nat. Rev. Microbiol. 21 (2023) 280–295.